Aerodynamic characterization of a soft kite by in situ flow measurement

Johannes Oehler[1] and Roland Schmehl[1]

[1]Faculty of Aerospace Engineering, Delft University of Technology, 2629 HS Delft, Netherlands

Correspondence to: Roland Schmehl r.schmehl@tudelft.nl

Abstract. Wind tunnel testing of large deformable soft kites for wind energy conversion is practically not feasible. Computational simulation of the coupled fluid-structure interaction problem is scientifically challenging and of limited practical use for aerodynamic characterization. In this paper we present a novel experimental method for aerodynamic characterization of flexible membrane kites by in situ measurement of the relative flow, while performing complex flight maneuvers. We find that

5 the measured aerodynamic coefficients agree well with the values that are currently used for flight simulation of soft kites. For flight operation in crosswind maneuvers where the traction force is kept constant, the angle of attack and the apparent flow velocity exhibit opposite trends. For entire pumping cycles, the measurements show considerable variations of the aerodynamic coefficients, while the angle of attack of the kite varies in fact only in a narrow range. This finding questions the commonly used representation of aerodynamic coefficients as sole functions of the angle of attack and stresses the importance of aeroelastic

10 deformation for this type of wing. Considering the effect of the power setting (identical to the trim) solely as a rigid-body pitch rotation does not adequately describe the aero-structural behavior of the kite. We show that the aerodynamic coefficients vary as functions of the power setting (trim) of the kite, the steering commands and flight direction.

1 Introduction

Airborne wind energy is the conversion of wind energy into electrical or mechanical power by means of flying devices. Some

15 of the pursued concepts use tethered airplanes or gliders, while others use flexible membrane wings that are derived from surf kites or parafoils (Diehl et al., 2017). The present paper is focusing on an airborne wind energy system (AWES) with an inflatable membrane wing that is controlled by a suspended cable robot (van der Vlugt et al., 2013, 2018). Compared to rigid-wing aircraft, the aerodynamics of tethered-membrane wings are not so well understood and kite development still relies heavily on subjective personal experience and trial and error processes (Breukels, 2011; Dunker, 2013). One reason for

20 this is the aeroelastic two-way coupling of wing deformation and air flow which can cause complex multi-scale phenomena. Another reason is a lack of accurate quantitative measurement data to support the design process. Soft kites such as leading edge inflatable (LEI) tube kites are highly flexible and have no rigid structure to mount sensors for precise quantification of the relative flow in the vicinity of the wing. This is why many experiments rely on ground-based force measurements and position tracking of the kite. In these experiments the environmental wind velocity introduced substantial uncertainties (Hummel, 2017;

25 Python, 2017).

With dimensions in the order of several meters, large surf kites or even larger kites for power generation exceed the size capacity of wind tunnels. Downscaling a physical model, as it is customary for rigid-wing aircraft, would require a synchronous scaling of the aerodynamic and structural problems, which for a fabric membrane structure with seams, wrinkles, multiple functional layers and integrated reinforcements is practically very difficult, if not unfeasible. A first full-scale experiment to

5   determine the shape of a kite in controlled flow conditions was performed by de Wachter (2008). Using photogrammetry as well as laser light scanning the three-dimensional surface geometry of a small ram-air surf kite was measured in two larger wind tunnels. This geometry was used as boundary condition for computational fluid dynamic (CFD) analysis of the exterior flow. The results show a substantial deformation of the membrane wing by the aerodynamic loading. Due to the difficulty of scaling, these results can not be transferred to larger kites for wind energy conversion that fly at higher speeds.

10   In general, the numerical simulation of strongly coupled fluid-structure interaction (FSI) problems is computationally expensive. If the flow is fully attached, standard panel methods with viscous boundary layer models can be used for efficient calculation of the aerodynamic load distribution. While this approach works, for example, for ram-air wings at lower angle of attack, it is not feasible for leading edge inflatable (LEI) tube kites because of the inevitable flow separation region behind the leading edge tube. Breukels (2011) and Bosch et al. (2014) develop multibody and finite element models of LEI tube kites and

15   use an empirical correlation framework to describe the aerodynamic load distribution on the membrane wing as function of shape parameters. Bungart (2009) performs CFD analysis using the deformed shape of the kite measured by de Wachter (2008), however, these results can not be extrapolated to different kites. We conclude that without accounting for the aeroelasticity of the membrane wing an accurate aerodynamic characterization does not seem to be feasible. We further conclude that presently experiments seem to be the most viable option to determine the global aerodynamic characteristics of a kite.

In Table 1 we list experiments described in literature to determine the lift-to-drag ratio of kites. The relative flow velocity

Table 1. Experimental methods for determining the lift-to-drag ratio of soft kites.

method	kite type	size [m^2]	limitations	wing loading [N/m^2]	v_a [m/s]	relative power setting u_p [-]	L/D [-]	reference
rotating arm	C-Quad	3.2	kite size, forces	100	11	low	4.9	Stevenson et al. (2005)
towing test	C-Quad	3.2	unknown wind	–	–	low	4.6–5.6	Stevenson et al. (2006)
wind tunnel	ram air	6	kite size	25	8	low–high	6	de Wachter (2008)
wind tunnel	ram air	6	kite size	60	12	low–high	6.7–5.7	
wind tunnel	ram air	6	kite size	120	16	low–high	8–5.5	
crosswind	ram air	6	kite size, forces	300	24	high	6.1	van der Vlugt (2009)
towing test	ram air	3	kite size, forces	30	8	–	6	Dadd et al. (2010)
towing test	LEI	15.3	force/speed limited	40	14	–	4.5–5.5	Costa (2011)
crosswind	LEI	14	wind data unknown	140	–	high	6	Ruppert (2012)
towing test	LEI	14	force/speed limited	40	11.3	low–high	4–10	Hummel (2017)

at the wing is denoted as v_a and the power setting u_p describes the symmetric actuation of the rear suspension lines of the kite. A high value of u_p means that the wing is powered, while a low value of u_p means that the wing is depowered. The variety of methods, test conditions and kites as well as generated results makes it difficult to derive a clear trend. Hobbs (1990) conducted a performance study of different single-line kite designs used for wind anemometry. A first quantitative aerodynamic assessment method for power kites was presented by Stevenson (2003), Stevenson et al. (2005) and Stevenson and Alexander (2006). The test procedure involves flying kites on a circular trajectory indoors as well as outdoor towing tests.

A similar manual test procedure for determining the lift-to-drag ratio of a surf kite was proposed by van der Vlugt (2009). The kite is flown in horizontal crosswind sweeps just above the ground, measuring the achievable maximum crosswind flight speed $v_{k,\tau}$ of the kite at a downwind position together with the wind speed v_w. Assuming that the measured wind speed is identical with the wind speed at the kite, the lift-to-drag ratio can be calculated from (Schmehl et al., 2013)

$$v_{k,\tau} = \frac{L}{D} v_w. \tag{1}$$

The method can be generalized to characterize the aerodynamics of kites flying complex maneuvers by measuring the unperturbed relative flow velocity v_a in the vicinity of the wing. Figure 1 shows a self-aligning Pitot tube setup mounted in the bridle line system between kite and its control unit. The placement of the Pitot tube in the bridle line system was chosen to avoid
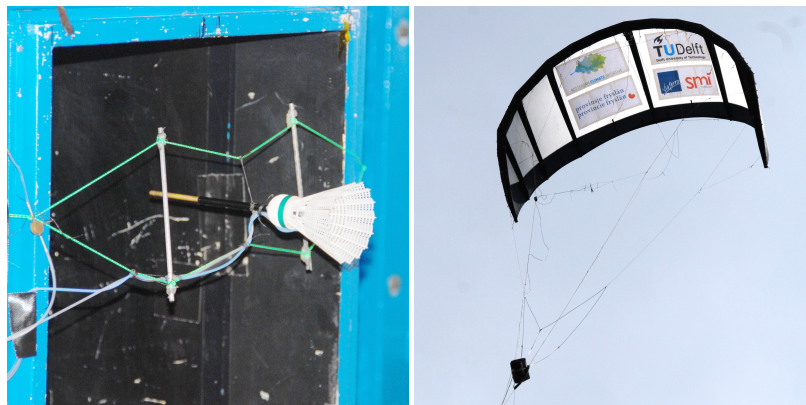
Figure 1. Pitot tube during calibration in the wind tunnel (left) and suspended in the bridle line system of a remote-controlled 25 m^2 LEI V2 kite during a flight test (right).

a perturbation of the relative flow by the wing and the control unit. However, Ruppert (2012) concluded that the quality of the measurement data of this setup was insufficient and thus estimated the wind speed at the kite from other available data. In lack of reliable velocity measurements, van der Vlugt et al. (2018) describe an approach to estimate the lift-to-drag ratio of the airborne system components from measured force and position data. Borobia et al. (2018) have mounted a Pitot tube directly on the center strut of a small surf kite to measure the relative flow speed. Together with the data of other onboard sensors, this has been used to feed an extended Kalman filter to get an optimal estimate of the relative flow velocity vector and other kite state variables.

Dadd et al. (2010) and Costa (2011) used towing test setups to generate a variable relative flow at the wing. Operating at days with calm wind allows for measurements at well-defined relative flow conditions. Hummel (2017) developed a similar trailer-mounted towing test setup to measure the lift-to-drag ratio and aerodynamic coefficients of surf kites. The test procedure includes active depowering, which, in general aerospace engineering terminology is denoted as a change in trim of the wing

5   and measuring line angles at the test rig. For future experiments, Hummel recommends the use of an airborne flow sensor to avoid the uncertainties caused by the wind environment and by the sagging of the tether.

The companies Kitepower, a startup of Delft University of Technology, Kite Power Systems (KPS) and Skysails Power (Weston, 2018) are currently developing and testing AWES with soft kites that are operated on a single tether and controlled by a suspended cable robot. These prototypes have reached considerable sizes (see for example Fig. 2) and for this reason

10   the use of measurement data acquired during flight operation is the only viable option for characterizing the aerodynamics of the complete airborne system. None of the other experimental setups presented in Table 1 allows to execute dynamic flight

Figure 2. LEI V5.40 kite with 40 m^2 wing surface area controlled by a suspended cable robot. This prototype temporarily reached a tether force of 15 kN and a mechanical power of 100 kW during a test flight in May 2018 (Kitepower, 2018).

maneuvers and handle kites with a wingspan of 10 m or larger, at flight speeds above 20 m/s while withstanding tensile forces of several kN or more. It is the objective of the present study to develop an experimental method for aerodynamic characterization of large deformable membrane kites that are used for energy conversion. At the core of this method is a novel setup for the

15   accurate measurement of the relative flow conditions at the kite during energy-generation in pumping cycles. Since the setup is additional equipment for tests of a commercial prototype the mounting of the setup has to consume as little time as possible.

The paper is organized as follows. In Sect. 2 we describe the airborne components of the kite power system, the measurement setup and the data acquisition procedure. In Sect. 3 we describe how the power setting is related to the angle of attack of the wing and how the aerodynamic properties are derived from the measured data. In Sect. 4 the results are presented and discussed.

2 System description and data acquisition

The experimental study is based on the AWES prototype developed and operated by the company Kitepower as a test platform within the EU Horizon 2020 "Fast Track to Innovation" project REACH (European Commission, 2015). The prototype can be classified as a ground-generation AWES, operating a remote-controlled soft kite on a single tether. This general setup is illustrated schematically in Fig. 3 (right). The main system components are the ground station for converting the linear traction
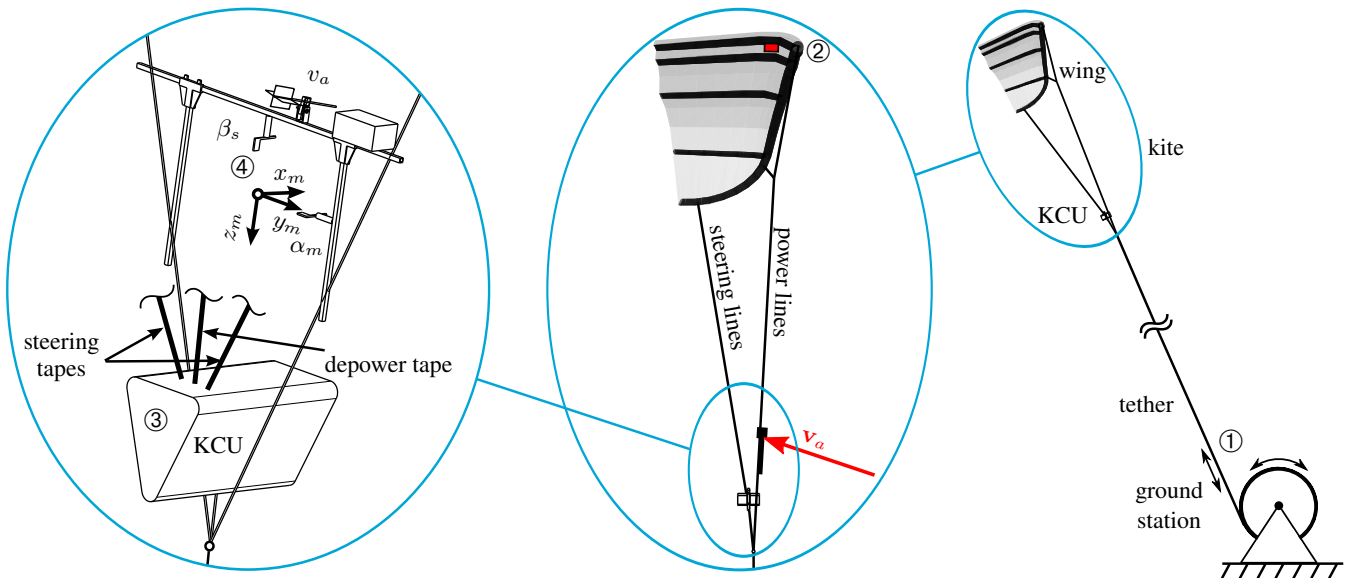
Figure 3. Basic components of the kite power system (right), wing with suspended control unit, together denoted as kite (center), and measurement frame attached to the power lines (left). Sensor positions: tether force F_t and tether reel-out speed v_t are recorded at the ground station ①, GPS and IMU modules are mounted on the center strut of the kite ②, the kite control unit ③ actuates the wing for steering and changing its power state, measuring also the instantaneous lengths of steering and depower tapes, the relative flow sensors for inflow angles α_m, β_s and apparent wind speed v_a are mounted on a rigid frame ④ that is attached to the two power lines connecting to the inflatable leading edge tube of the wing.

motion of the kite into electricity, the main tether and the C-shaped, bridled wing with the suspended kite control unit (KCU). In the following we will denote the assembly of wing, bridle line system and KCU as "kite". To generate power the kite is operated in cyclic flight patterns with alternating traction and retraction phases. During the traction phase the kite performs crosswind maneuvers, while the tether is reeled off a drum that is connected to a generator. In this phase the kite generates

10 electricity. For the subsequent retraction phase the crosswind maneuvers are stopped and the generator is operated as a motor to reel in the tether. This phase consumes some of the generated electricity. To maximize the net gain of energy per cycle the wing is depowered during retraction. Both steering lines are released evenly such that the tips of the wing pitch rotate to a lower angle of attack, which significantly reduces the aerodynamic lift force.

Just below the KCU the main tether splits into two power lines of constant length that run along the sides of the KCU and support the inflatable leading edge tube and partially also the strut tubes of the wing. This is depicted schematically in Fig. 3 (center and left) and in more detail in Fig. 5 (left) without the measurement setup. A short line segment connects the KCU to the end point of the main tether, while steering and depower tapes connect the KCU to the steering lines and eventually, via a

5   fan of bridle lines, to the wing tips and trailing edge. Details on this specific layout will be described in the following section. The KCU can actuate the two steering lines either symmetrically, to power and depower the kite, or asymmetrically, to steer the kite. The actuation of the wing as part of the kite is illustrated in Fig. 4. The photographic footage from 23 August 2012
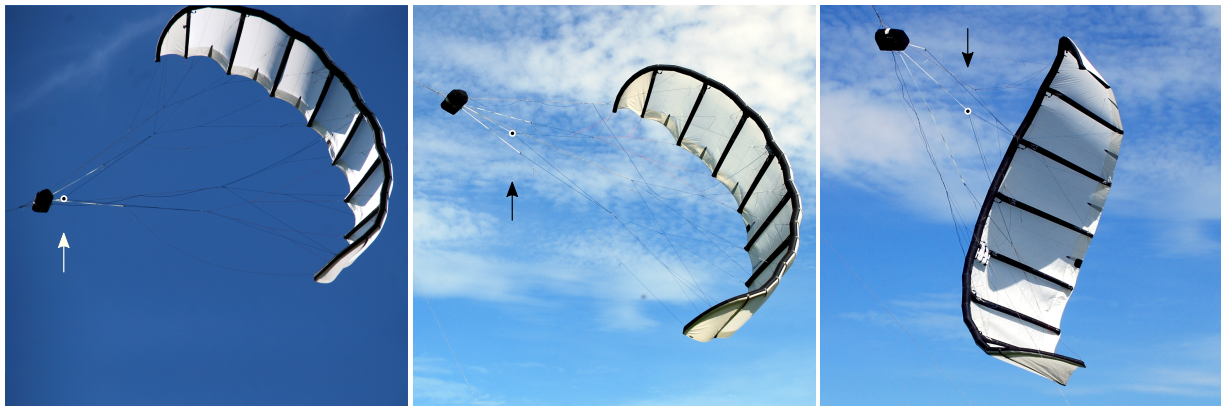
Figure 4. Almost fully powered kite (left), depowered kite (center) and deformation of the wing by extreme steering input in depowered state (right). Dots indicate the end of the depower tape.

is documenting tests of a mast-based launch setup. While the left photo is taken during crosswind maneuvers during power generation, the two right photos are taken during a flight maneuver close to the launch mast.

10   The sensors on the ground station ①, the kite ② and the KCU ③ provide data that is required for the autopilot of the kite power system (see Fig. 3). The experiments described in this paper have been performed with a LEI V3 kite with a wing surface area of 25 m^2, a battery-powered KCU for 2–3 hours of continuous operation and a ground station with 20 kW nominal traction power. These components have been developed by the kite power research group of Delft University of Technology and reflect the technology status in 2012 (van der Vlugt et al., 2013; Schmehl, 2014; Schmehl et al., 2014; van der Vlugt et al., 2018).

15   Because the membrane wing is continuously deforming during operation it is not as straightforward as for a rigid-wing aircraft to define the orientation of the kite relative to the flow. One option is to use the inflated center strut as a reference component to mount the flow measurement equipment (van Reijen, 2018; Borobia et al., 2018). Mounting the equipment directly on the suspended KCU is not considered to be an option because this relatively heavy component is deflected substantially when flying sharp turns (Fechner and Schmehl, 2018) and can also exhibit transverse vibrations. Another option is to mount

20   the measurement equipment on the two power lines. These lines transfer the major part of the aerodynamic force from the wing to the tether and for this reason are generally well-tensioned and span a plane that characterizes the orientation of the kite

(wing and suspended KCU). Considering the deformation of the membrane wing by asymmetric and symmetric actuation as well as aeroelasticity, we consider this plane to be the most suitable reference geometry.

Figure 3 (left) illustrates how the three relative flow sensors ④ are mounted on a rigid frame that is attached to the two power lines about 8.5 m below the kite. In Appendix A we use a simple lifting-line model of the wing to show that the assumption

5 of free stream conditions at this distance from the kite is justified. The Pitot tube can rotate freely to align with the relative flow, measuring the barometric pressure, the differential pressure and the temperature from which the apparent wind velocity v_a can be calculated. The two flow vanes are used to determine the inflow angles α_m and β_s which are measured from the normal vector of the plane spanned by the two power lines. The two angles are measured by total magnetic encoders with a resolution of $0.35°$. The data is recorded at a frequency of 20 Hz, converted to a digital signal by a Pixhawk® microcomputer,

10 transmitted to the KCU and from there to the ground station to be logged simultaneously with all other acquired sensor data. It is important to note that the relative flow sensors are add-on measurement equipment for the present study and are not essential for the operation of the kite power system. More information on the sensors and the measurement setup can be found in Oehler (2017).

The new setup addresses two shortcomings of the earlier attempts to determine the relative flow conditions at a kite, il-

15 lustrated in Fig. 1. Firstly, a self-aligning Pitot tube alone can measure only the magnitude of the relative flow velocity but not its direction. The orientation of the wing relative to the flow is however an important information for the aerodynamic characterization. Secondly, the tensile suspension of the Pitot tube in the bridle system of the kite was not sufficiently robust against perturbations which negatively affected the quality of the measurement results. Jann and Greiner-Perth (2017) describe a similar setup for gliding parachutes, mounted in the bridle lines between payload and wing, to measure the angle of attack

20 and relative flow speed. By choosing a setup that is flying with the kite we are able to acquire the relative flow conditions in situ, during operation of the full-scale system, and are not constrained by the traction force limit of a particular ground testing rig. This allows us to characterize also the aerodynamics of power kites that produce much more lift force than usual surf kites. In the following we denote the airborne wind energy system onboard measurement equipment by the acronym AWESOME.

3   Data processing

25 The raw data from the rotary encoders and the pressure sensor can have missing data points and can also fluctuate due to variations of the supply voltage. To address these issues we apply a moving-average filter, using the Matlab® function *smooth* with a span of 7 measurement points (0.3 s). This operation returns a smooth signal while still being able to capture systematic oscillations that occur at frequencies of up to 1.2 Hz (Oehler, 2017). In the following we describe how the relative flow data is used together with the data of the other sensors to determine the aerodynamic properties of the kite.

30 ### 3.1   Geometry and reference frames

The geometry of the wing and the layout of the tensile support system, comprising bridle lines, steering and depower lines, as well as steering and depower tapes are illustrated in Fig. 5. The two pulleys are attached to the two branches of the rear bridle
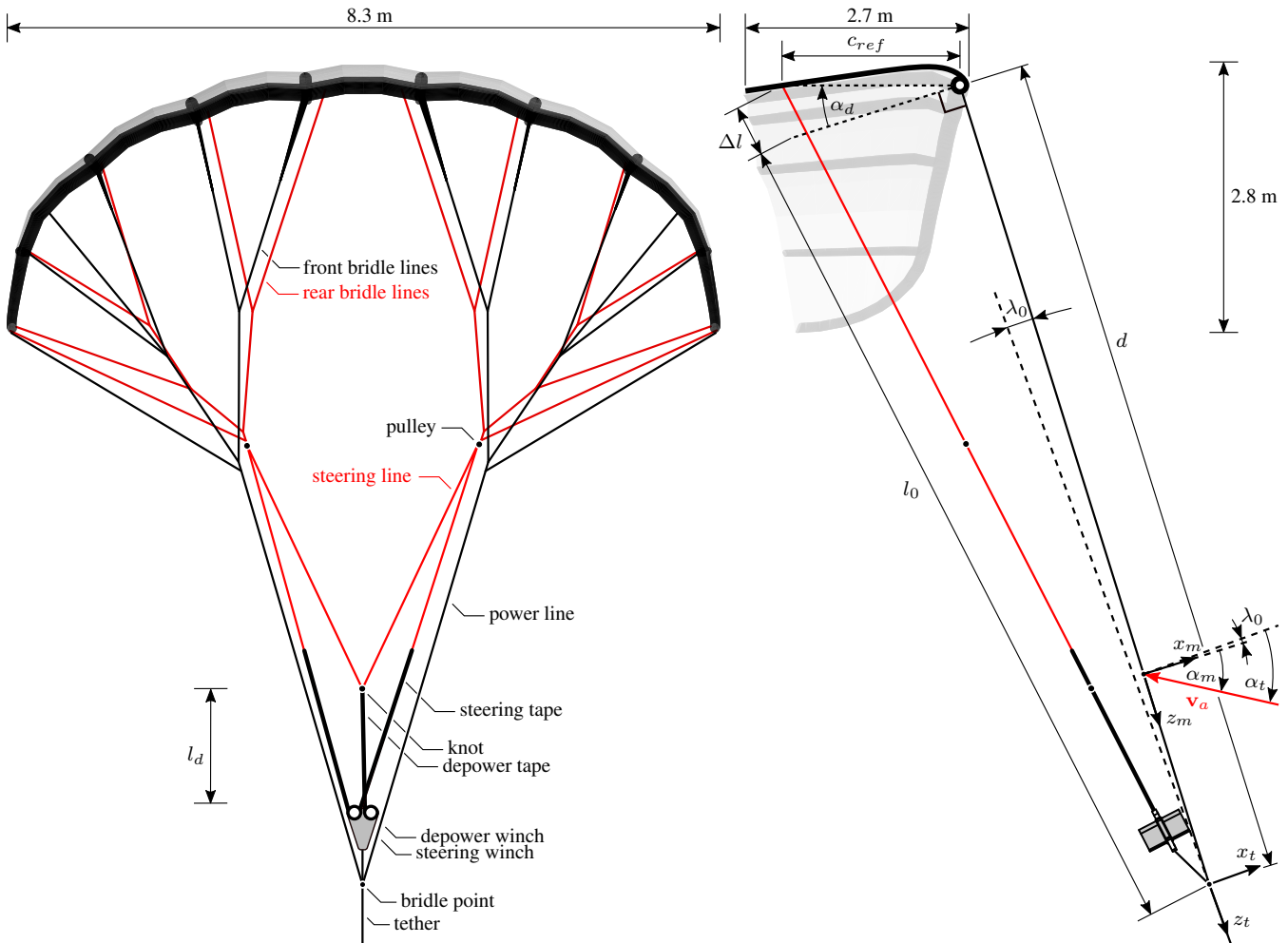
Figure 5. Front view (left) and side view (right) of the kite with reference frames, geometric parameters and definition of the reference chord c_{ref}. The explicit dimensions describe the unloaded design shape of the wing.

line systems and allow the steering lines to slip freely to adjust the line geometry to the actuation state. The instantaneous length of the depower tape is denoted as l_d. Both views show a depowered kite, as illustrated in Fig. 4 (center).

As shown in Fig. 5 (right), we define two different reference frames to describe the orientation of the tether and the kite. The tether reference frame (x_t, y_t, z_t) is attached to the airborne end of the tether with its origin at the bridle point where the tether splits into the two power lines. The z_t-axis is tangential to the tether, while the x_t-axis is located in the plane spanned by the z_t-axis and the normal vector of the plane spanned by the two tensioned power lines. This definition is identical to the "kite reference frame" used by Fechner et al. (2015) as a basis for a point mass model. The measurement reference frame (x_m, y_m, z_m) is attached to the rigid frame on which the relative flow sensors are mounted. As depicted in Fig. 3 (left), the z_m-axis is aligned with the two upright members of the frame, while the y_m-axis is aligned with the transverse member. Because

the measurement frame is attached to the two tensioned power lines the x_m-axis defines the heading of the kite. The rotation of the x_t-axis into the x_m-axis is described by λ_0. This angle can not be controlled actively, but a result of the kite design and bridle layout and of the forces acting on the wing.

The inflow angles β_s and α_m are determined in the measurement reference frame. Because the z_m-axis can be regarded as the yaw axis of the kite, the inflow angle β_s is equivalent to the side slip angle. Similarly, the y_m-axis can be regarded as the pitch axis of the kite and the inflow angle α_m is a measure for its pitch orientation with respect to the flow. To transform α_m into a meaningful angle of attack of the wing we need to define a reference chord. The common practice of using the center chord as a reference seems hardly useful because the wing deformation during flight makes it questionable whether the center chord is representative for the entire wing. Instead, we use the plane spanned by the power lines as a reference. We define the reference chord c_{ref} to be perpendicular to this plane for the fully powered kite. While this definition appears arbitrary at first it is in fact a reasonably good approximation for the center chord of the investigated kite design because the fully powered kite is designed for optimal load transfer from membrane wing to tensile support system. These structural requirements are generally met best if bridle lines connect perpendicularly to the tubular frame of the wing. This is illustrated by the almost fully powered kite in Fig. 6, showing a photographic snapshot from the same sequence that was also used for Fig. 4 (left). The point of observation is several hundred meters away and roughly in the $y_t z_t$-plane of the kite. It is clearly visible from the center strut of the kite that the chord is approximately perpendicular to the front bridle lines.[1] The photo also visualizes the angle λ_0 between front bridle lines and tether.

Figure 6. Almost fully powered kite from the ground.

The video stills in Fig. 7 indicate how the wing shape changes when transitioning from depowered to powered state. The GoPro® video camera with ultra-wide angle "fisheye" lens captures the entire wing and bridle line system, from which we can make several qualitative comparisons. It is obvious that the powering of the wing tensions the entire bridle line system such that the two pulleys (marked by circles) move forward, towards the leading edge. The increasing projected center chord indicates that the wing pitches into the projection plane. The slightly increasing projected span indicates that the entire wing straightens under the substantially increased aerodynamic loading when being powered. Also the curvature (sweep) of the leading edge

---

[1]It is straightforward to account for an offset angle between the reference chord of the fully powered kite and the normal vector of the power line plane, as proposed by Fechner et al. (2015). Because this offset angle α_0 is difficult to determine experimentally we have omitted it in the present analysis, assuming, per definition, that $\alpha_0 = 0$.
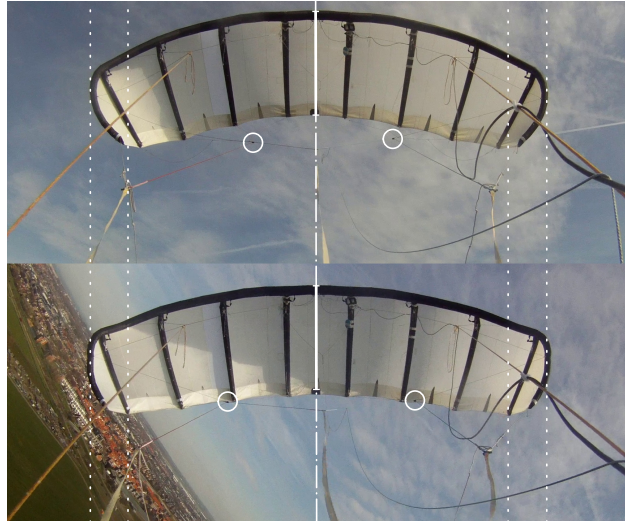
Figure 7. Depowered kite (top) and powered kite (bottom) from a video camera mounted on the KCU and looking into the wing.

tube slightly decreases. It is clear that all these effects can not be taken into account in a mechanistic model without describing the entire fluid-structure interaction problem, including membrane wing, bridle line system and steering actuation. For this reason we resort to a simple pitch-rotation model of the depowering maneuver.

The geometric model to describe the orientation of the reference chord with respect to the power line plane is illustrated in
5   Fig. 5 (right). The length d describes the distance from the bridle point to the leading edge of the wing, while the length l_0 describes the distance from the bridle point to the rear end of the reference chord of the fully powered kite. Because the front and rear bridle lines connect to the inflatable tubular frame inwards of the leading and trailing edges of the wing, the reference chord is shorter than the aerodynamic chord at midspan, which is 2.7 m.

The depowering of the kite is quantified by the actuation length Δl and the depower angle α_d, which was already introduced
10   by Fechner et al. (2015). Based on these considerations, the angle of attack of the relative flow with respect to the reference chord is defined as

$$\alpha = \alpha_m - \alpha_d, \tag{2}$$

while the angle of attack of the relative flow with respect to the tether is given by

$$\alpha_t = \alpha_m + \lambda_0. \tag{3}$$

15   **3.2   Kinematics of depowering**

To maximize the net energy of a pumping cycle, the lift coefficient C_L and the lift-to-drag ratio L/D of the kite have to be minimized during the retraction phase. This is achieved by increasing the distance between the bridle point and the rear end of the reference chord to $l_0 + \Delta l$, which is formally expressed also as a reduction of the power setting u_p. Instead of assuming a

linear correlation between u_p and the depower angle α_d, as proposed in Fechner et al. (2015), we derive the correlation from the pitch rotation of the reference chord illustrated in Fig. 5 (right). Using the cosine law we calculate the depower angle α_d from

$$\cos(90° + \alpha_d) = \frac{d^2 + c_{ref}^2 - (l_0 + \Delta l)^2}{2dc_{ref}}. \tag{4}$$

5   The geometrical data is extracted from the CAD model of the LEI V3 kite. The distance from bridle point to leading edge of the wing is $d = 11.0$ m, while for the fully powered kite the distance from bridle point to the rear end of the reference chord is $l_0 = 11.22$ m. The length of the reference chord is $c_{ref} = 2.2$ m. Considering the specific layout of the actuation system depicted in Fig. 5 (left), the extension of the rear suspension of the reference chord is calculated as

$$\Delta l = \frac{1 - u_p}{2} l_{d,max}, \tag{5}$$

10   where $l_{d,max} = 1.7$ m is the deployable length of the depower tape. Because we use a pulley system to decrease the required forces in the actuation system, only half of the length of the depower tape is translated into lengthening or shortening the rear suspension of the reference chord. Consequently, Eq. (5) results in a maximum extension $\Delta l_{max} = 1/2 l_{d,max}$ for full depowering of the wing with $u_p = 0$, while Eq. (4) gives a maximum depower angle of $\alpha_{d,max} = 24°$.

In this work, the wing is treated as lifting surface with a fixed geometry that is pitch rotated relative to the power lines by
15   lengthening and shortening the depower tape. On the other hand, a pitch rotation of the entire kite, i.e. the assembly of wing and KCU, around the bridle point has no effect on the relative orientation of the lifting surface. This kinematic model is a simplified two-dimensional approximation of the complex three-dimensional aeroelastic behavior of the bridled membrane wing. At the present state of knowledge the strong fluid-structure coupling can not be described by an analytic model.

3.3   Lift-to-drag ratio as function of tether angle of attack

20   A common method to estimate the lift-to-drag ratio of a kite is to measure the tether elevation angle β with the horizontal at static flight (Stevenson, 2003). However, this method introduces uncertainties arising from the tether sag and the usually unknown wind conditions at the position of the kite. Further, the method is unsuitable for analyzing dynamic flight maneuvers. Stevenson (2003) introduces the tether angle of attack α_t to account for all forces acting on the kite components above the bridle point, in our case, the KCU, the bridle line system and the wing. Defined by Eq. (3), this angle is thus of high interest
25   for describing the aerodynamics of the kite. But the value changes with the flight situation. To derive the purely aerodynamic lift-to-drag ratio L/D we need to take into account the effect gravity has on the force equilibrium of the kite. Figure 8 shows all forces acting on the kite lumped into the bridle point. The lift-to-drag ratio can be calculated as

$$\frac{D}{L} = \tan(\alpha_t - \Delta\alpha). \tag{6}$$

Since the model integrates all forces above the bridle point, the aerodynamic coefficients L/D and C_L are always given for the
30   whole kite as entity of canopy, bridle lines and KCU. $\Delta\alpha$ accounts for the influence of the kite's weight. It can be calculated
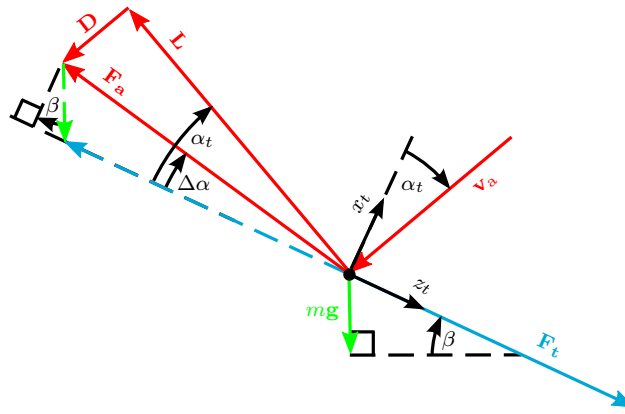
Figure 8. Deriving aerodynamic lift-to-drag ratio L/D from tether angle α_t. In this sketch all forces acting on the airborne system are lumped to the bridle point with the kite flying upward (heading angle $\chi = 0°$). Dashed vectors are copies of weight (green) and tether force (blue) to illustrate geometric relations but do not represent actual forces.

by

$$\tan(\Delta\alpha) = \frac{mg\cos\beta\cos\chi}{F_t + mg\sin\beta}, \tag{7}$$

assuming a force equilibrium of aerodynamic force F_a, tether force F_t and weight, using the mass of the kite of $m = 22.8$ kg, the elevation angle β and the heading angle χ. The heading angle χ is defined as the angle between local upward in the

5   plane perpendicular to the connection line from ground station to kite and the projection of x_t on this plane. When flying horizontally with a heading angle of $\chi = \pm90°$ gravity influence is offset by a sideslip angle (Fechner and Schmehl, 2018). For heading angles indicating upward flight $\chi \in (-90°; 90°)$, we obtain positive values for $\Delta\alpha$, for the opposite case gravity has a component in the direction opposing the wing's drag which results in a negative value for $\Delta\alpha$. β is the kite's elevation angle which is obtained from the position of the kite with respect to the ground station. Sagging of the tether is neglected, as the

10 tether being straight, sagged, long or short does not directly affect the measurement of L/D which is one of the key advantages of this measurement method over angular measurements on the ground (Hummel, 2017). The absolute value of the tether force plays a role only in so far that it changes the ratio of weight to tether force in Eq. (7).

To obtain α_t from the measurements, it is apparent from Eq. (3) that the angle between main tether and power lines λ_0 is required. This angle is calculated by solving the substituted mechanical system in Fig. 9 for its kinematic equilibrium position.

15 We thereby assume that the kite flies in a quasi-steady equilibrium (van der Vlugt et al. (2018); Oehler and Schmehl (2017)). Inputs are the tether force F_t acting in direction of z_t at the bridle point, the individual weight contributions of KCU, wing and AWESOME and the estimated drag forces of KCU and AWESOME. Considering blunt bodies with $C_{D,blunt} = 1.0$ their drag contribution is about 10% (KCU) and 1% (AWESOME) of the wing drag. From these five forces we calculate the resultant aerodynamic force of the wing $F_{a,w}$ which is necessary for a non-accelerated flight situation with force equilibrium. The model

20 with a point mass for KCU and straight power lines and rear suspension lines is similar to the one described in Bosch et al.

(c) Author(s) 2018. CC BY 4.0 License.
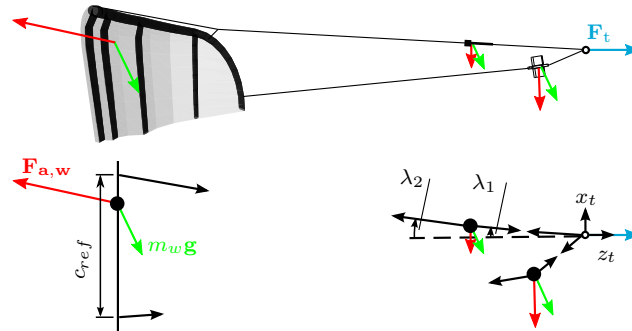
Figure 9. Substituted mechanical system of wing and KCU with external and internal forces for the calculation of the bridle lines' angles λ_1 and λ_2.

(2013). All forces are acting at the same place as their related point masses (see Fig. 9). We assume both center of pressure and center of mass of the wing at 25% of the reference chord length. This is in line with Bosch's estimate for the center of mass and a force ratio of one third for a high power setting in Hummel (2017).

Both van Reijen (2018) and Hummel (2017) observe a shift in the center of pressure for different power settings. When the
5   kite is powered up thus the rear suspension lines shortened, the pressure point moves backwards. As we do not measure the difference in forces on the front bridle lines and rear bridle lines we cannot account for this shift in center of pressure. The effect is different for every kite/bridle combination but a ratio of 3:1 for the forces in front and back bridles seems like a good average value.

The tether sag does not need to be calculated and does not affect the calculation which is a big advantage over ground based
10   measurements (e.g. angular sensors at the tether exit point of the ground station). The influence of the aerodynamic senors' weight was found to be negligible. The cause for this is that AWESOME is much smaller than the KCU and the traction force transferred by the power lines where it is installed is three times larger than the force in the rear suspension lines. λ_1 and λ_2 differed by only 0.1 or 0.2° so the power lines are considered straight, we use the mean value of both λ_1 and λ_2 as λ_0. The KCU in contrast has a considerable effect, especially during reel-in maneuvers when the force in the rear suspension lines is of
15   the order of the KCU's weight.

The calculated values vary between $\lambda_0 = 0 - 2°$ for flying downward. For upward flight and during reel-in we find values of $\lambda_0 = 3 - 7°$. For low tether tension and upward flight values of 10–12° occur. This shows why a constant λ_0 cannot be assumed. The highest values occur when both tether tension and elevation angle are low which happens during launch and landing.

20   Generally the pitching of the kite around its attachment point does not change the bridle geometry. This is the case when all lines are tensionned and can be assumed straight. However this is not always true for the lines connecting trailing edge to KCU and main tether. When flying upward during power production the KCU's drag and weight act in the same direction (downward), the back lines connecting to the trailing edge are deviated from being straight and consequently shortened. This can be modeled as a negative depower angle α_d.

3.4 Deriving the lift coefficient C_L

With

$$L = \frac{1}{2}\rho C_L v_a^2 A \tag{8}$$

we can determine the kite's lift coefficient C_L. Density ρ and apparent flow velocity v_a are measured directly, the projected wing surface area $A = 19.75 \text{ m}^2$ is known. Using the kite's lift-to-drag ratio L/D and the known influence of gravity we can compute the lift force generated by the kite as

$$L = F_a \sqrt{\frac{\left(\frac{L}{D}\right)^2}{1 + \left(\frac{L}{D}\right)^2}}. \tag{9}$$

The resultant aerodynamic force of the airborne system F_a can be calculated from the tether force F_t, the elevation angle β and the kite mass m (see Fig. 8)

$$F_a = \sqrt{(F_t \cos\beta)^2 + (F_t \sin\beta + mg)^2}. \tag{10}$$

4 Results
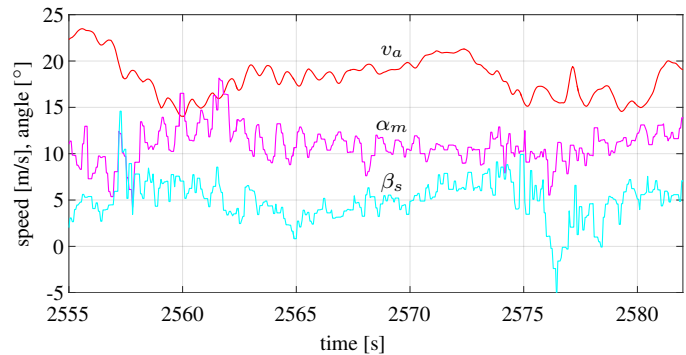
Figure 10. Photo of the in situ measurement setup (left), diagram showing raw values of apparent flow velocity v_a and inflow angles over time during an exemplary traction phase (right).

Data was collected during a one hour test flight of the prototype system described in Sect. 2 on 24 March 2017 at the former naval airbase Valkenburg, close to Leiden, the Netherlands. A camera mounted on AWESOME provided proof that all sensors were moving freely in the airflow and did not show any visible faulty behavior (see Fig. 10). The plot shows the first 30 s of one representative traction phase. In all plots with time on the horizontal axis the launch of the kite corresponds to $t = 0$ s. The maximum speed occurs in the beginning of the plot, when the transition from reel-in to traction phase is happening and the kite is flying downwards. Gravity helps to accelerate the kite to a high velocity.

One first obvious result is that the measurement contradicts previous findings of Ruppert (2012) which indicate considerable variations in angle of attack of up to $30°$ during traction phase and also high angles of sideslip varying in $\beta \in [-20°, 20°]$. In the observed data set the angle of attack showed only minor variations between 6 to $16°$ during traction phase. The measured angle of sideslip deviates from its mean by a maximum of $\Delta\beta = 10°$ for very sharp turns. Estimation of the flow angles

5 without systematic flow measurement and estimation of the air speed at the kite's position from GPS/IMU data and ground based measurements only as conducted in Ruppert (2012) should be considered an insufficient way of determining a kite's flow field. The kite's speed lies around $v_a = 18$ m/s for the traction phase and below $v_a < 15$ m/s for retraction. In the analyzed experiment of March 24 the sideslip angle was not centered around a value of zero which we would expect for a symmetric kite. The reason for this was found in a non symmetric bridle setup which caused the kite to fly in a non symmetric pattern during

10 reel-out phase. To conduct a concise analysis of the influence of sideslip on the kite's aerodynamics a different experimental data set is needed.

4.1 Oscillation

The data in Fig. 10 shows strong fluctuations at a distinct frequency of $f_{GS} = 1.2$ Hz in both v_a and α_m. This oscillation occurs several times during reel-in and reel-out for periods of several seconds. The values of tether force F_t and reel-out speed

15 v_t, measured at the ground station, as well as pitch rate, forward and downward accelerations measured by the kite's inertial measurement unit (IMU) are other independent measurements showing the oscillation of the kite. In Oehler and Schmehl (2017) the strong damping of the kite system $\zeta_k = 0.63$ and its eigenfrequency for a pitch motion of $f_{k,traction} = 0.81$ Hz during traction phase and $f_{k,retraction} = 0.39$ Hz during retraction phase are found. The fact that the kite oscillates during traction and retraction phase with $f_{GS} \neq f_k$ leads to the conclusion that we do not observe a mode of the kite system but

20 a forced oscillation commanded by the ground station. Absence of this behavior whenever $v_t = 0$ supports the classification as forced oscillation that is governed by the control law of the ground station. This oscillation mode could be suppressed by adjusting the ground station controller, however this is not part of this work.

To estimate the effect of this oscillation on the flow field of the kite, the reduced frequency

$$k = \frac{f\pi c}{v_a} \tag{11}$$

25 as defined in (Hassig, 1971) is calculated. For the frequency of the oscillation $f_{GS} = 1.2$ Hz a chord length of $c = 2.7$ m and an apparent flow speed of $v_a = 20$ m/s the reduced frequency is $k_{GS} = 0.5$. This means we have to expect highly unsteady aerodynamic behavior. This can lead to a phase shift of the registered aerodynamic load with respect to the angle of attack. In order to minimize this effect, the data is smoothed over an interval of $T = 2.5$ s which is equivalent to 3 periods of the oscillation. In case a phase shift between angle of attack and aerodynamic force occurs, this should be compensated. This

30 smoothing rule renders the assumption of quasi-steady flight applicable for all flight phases except for turns where the kite is accelerated consistently.

For the figure of eight flight pattern we assume a characteristic frequency of $f_{turn} = 0.1$ Hz which corresponds to the turning maneuvers where the kite performs a half turn in about five seconds. For these flight maneuvers we obtain a reduced frequency of $k_{turn} = 0.042$ which is an indication that we can assume quasi-steady aerodynamics.

4.2 Lift-to-drag ratio
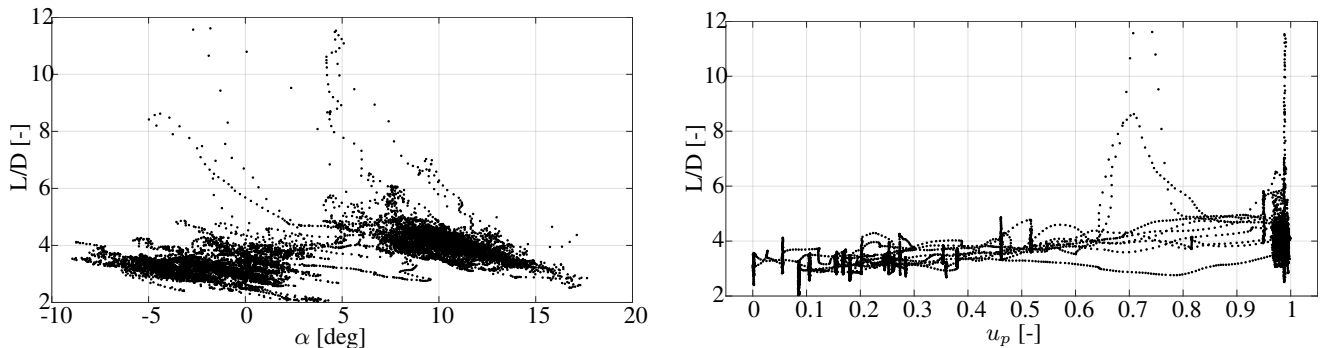
Figure 11. Raw data of lift-to-drag ratio plotted over angle of attack (left) and power setting of the kite (right). No filtering is applied to the data.

5   We choose two different ways to plot the lift-to-drag ratio L/D. First over the angle of attack defined in Eq. (2) which is customary for profiles and aircraft. Secondly we also plot L/D over the power setting u_p.

    Figure 11 shows the lift-to-drag ratio L/D plotted over the angle of attack α (left) and over the power setting u_p (right). The data points are scattered, because there are many variables with an effect on the lift-to-drag ratio such as angle of attack, power setting, aerodynamic force, steering input and angle of sideslip. In Fig. 11 only the models from Sect. 3 are used but no further

10 filtering is applied. It is apparent that there is a region where the kite flies at a low angle of attack in the range $\alpha \in [-7, 3]$ and one region with higher $\alpha \in [7, 15]$. Low angles of attack indicate the reel-in period, high angles of attack indicate the traction phase. On the right side the power setting u_p allows a clear separation between reel-in phase with $u_p < 0.55$ and reel-out phase with $u_p \approx 1$. Values in between mark the transition between both flight states. The lift-to-drag ratio lies around $L/D = 4$ for the traction phase and at a lower $L/D = 3$ during retraction which is what is desired to limit the traction force during reel-in.

15   To make this trend more visible in Fig. 12 a color code is used to indicate the power setting u_p. The smoothing rule described in Section (4.1) is applied to the data. We further assume that the high lift-to-drag ratios of up to $L/D = 12$, visible in Fig. 11 are not physical. In Fig. 12 data points with a tether force below $F_t = 400$ N are not plotted, which proofs that this is the cause for the unrealistically high lift-to-drag values. For low tether tension the model is not valid since it assumes straight tensioned lines and a quasi-steady state of the kite. Both should be doubted for low registered tether forces, since inertia of the wing and

20 KCU can not be neglected with respect to such a low force. This is why data points with low tether force are not shown for all further plots.

    In Fig. 13 L/D values are plotted with a color code indicating the strength of the steering input. Yellow and red colors indicate a very strong steering maneuver. It is visible that this coincides with the occurrence of low tether force and the extreme
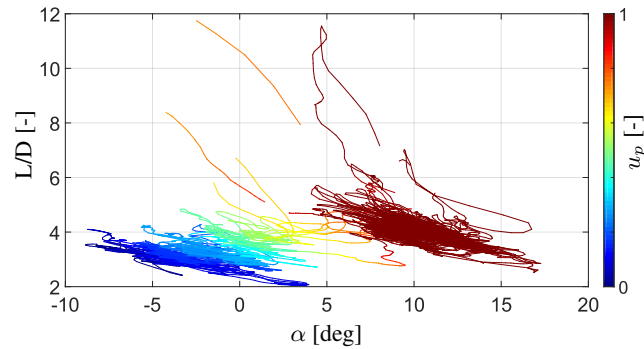
Figure 12. Lift-to-drag ratio with colors indicating the power setting u_p of the kite. Red stands for the highest power setting during traction phase $u_p = 1$, blue signifies low power setting during retraction.
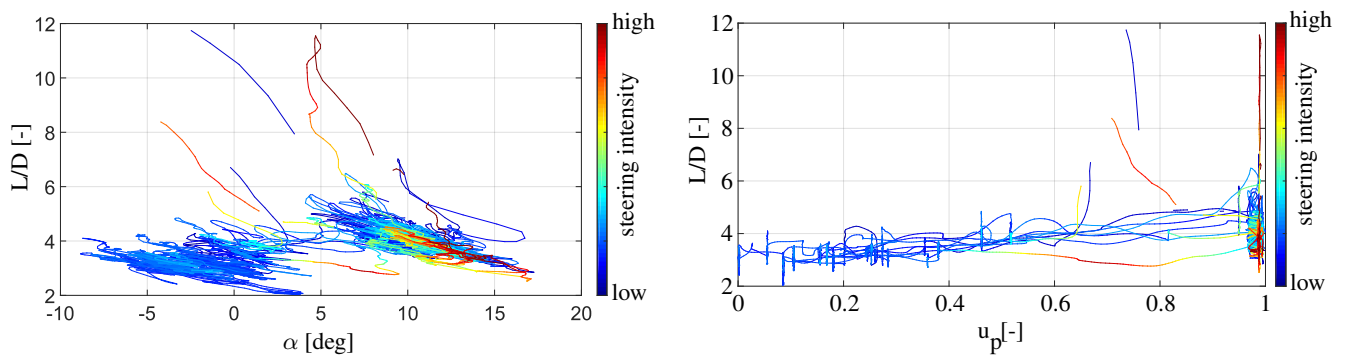
Figure 13. Effect of steering on the lift-to-drag ratio. Red color indicates a turning maneuver with strong steering tape deflection.

values of the lift-to-drag ratio L/D. To compare the experimental data with aerodynamic kite models we look at straight flight segments only and thereby exclude the effect of deformation during turning. That's why the data points with strong steering input are filtered. This yields the plot in Fig. 15 where all filters described in Table 2 are applied.

In all plots we see that for an increasing power setting u_p the angle of attack and also the lift-to-drag ratio increases. The

5   maximal lift-to-drag ratio of about $L/D = 5$ lies at an angle of attack of $\alpha \in [5°, 10°]$ and is only reached when the kite is at its highest power setting $u_p = 1$. For higher angles of attack L/D is lower again. For the plotted lift-to-drag ratio over the angle of attack we obtain the same trend we would expect for a conventional airfoil or aircraft. Low angles of attack produce small lift and therefore a low L/D, after reaching a maximum for an angle of attack of usually around $\alpha = 8°$ the lift-to-drag ratio drops again for higher values because of increased drag. The same trend was already observed in flight data analyzed by

10   van der Vlugt et al. (2013).

From Fig. 13 we see that steering maneuvers lower L/D. For the same power setting u_p, lift-to-drag ratios are significantly lower in traction and transition phase when the kite's steering is activated. This has been shown also in Oehler et al. (2018). The cause can be either the deformation of the wing when the length of the steering tape is changed or the flow vector coming from the side as a result of rotation and cornering of the kite. As both are happening at the same time it is hard to determine

which is the dominant cause, possibly both factors lead to an increase in drag and consequently a lower L/D value. Also there is a feedback loop because increasing drag lowers the L/D value which will increase α_t and to a certain extent also α. For higher α values we find a lower L/D value again.

Figure 14 shows the evolution of L/D over time, together with the power setting u_p. It shows clearly that changes of the power setting u_p have a dominant effect on L/D. During traction phase all drops below $L/D = 4$ occur at the same time than steering maneuvers. This is due to the deformation of the wing and the additional drag that makes steering possible (Fechner et al., 2015). For a comparison with aerodynamic models which assume straight flight the exclusion of all data points with a strong steering command is necessary.
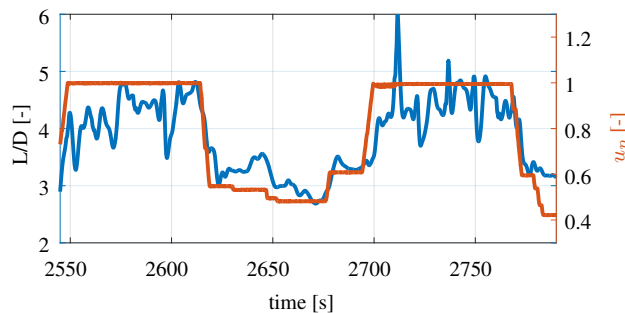
Figure 14. Evolution of the lift-to-drag ratio during pumping cycle flight.

4.3   Comparison with aerodynamic models

Two real-time capable models for simulation of a pumping kite power system were developed by Ruppert (2012) and Fechner et al. (2015). The aerodynamic models they use were modified from experimental data of two-dimensional sail wing experiments. Fechner et al. writes that they made experience based modifications to the aerodynamic models. In both cases major model adjustments were required to align simulation results with the flight experiments. Their justification is that they produce good simulation results and can trace the real flight path and power production in many flight situations. Both authors were not primarily focusing on aerodynamics of the kite but more on developing a model that works conveniently for a simulation of the flight path and optimization of kite control.

As they both use different definitions for the angle of attack, we have to assume an offset in this angle. Fechner et al. (2015) defines the angle from center chord to the flow vector as angle of attack, Ruppert (2012) uses the orientation of the IMU mounted on the wing towards the flow vector. Both values are hard to reproduce in a following measurement campaign as the airfoil's center chord orientation is generally unknown and only estimated. The IMU is mounted with Velcro tape on a strut of the wing which makes a reproducible orientation difficult, even when using the same kite.

To compare their models with the measured data of this experiment, both curves are transformed to have their maximal L/D value at $\alpha = 7.5°$ such as in the measured data instead of $\alpha_{L/D,max,Ruppert} = 12.5°$ and $\alpha_{L/D,max,Fechner} = 16°$.

Table 2. Filters applied to the data points of the lift-to-drag ratio.

filter	reason	visible effect
moving average over 2.5 s	oscillation GS; balance dynamic effects to make quasi-steady assumption applicable	reduces spread during reel-in
$F_t > 400$ N	model limitation	delete outliers
exclude steering	strong deformation	delete outliers
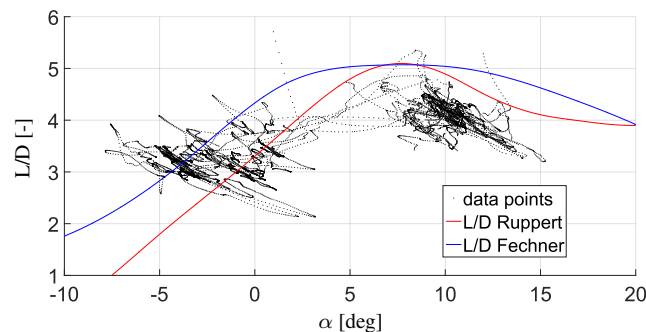
Figure 15. Comparison of measured lift-to-drag ratio with the aerodynamic models of Fechner et al. (2015) and Ruppert (2012).

Fechner et al. (2015) states that during steering maneuvers the L/D values are lower due to increased drag at the tips. Therefore the aerodynamic curves are only valid for straight flight. Ruppert (2012) in the same way excluded data points with strong steering inputs from his model for the aerodynamic performance. From the data in Fig. 14 it is apparent that a turning kite and a kite flying straight do not have the same L/D values. For this reason in Fig. 15 only data points without excessive

5   use of the steering capability are plotted. All the filters described in Table 2 are applied. Combining all these filters on the scatter plot from Fig. 11 yields Fig. 15.

We find a reasonable agreement of the measured data points with the aerodynamic models. Both models slightly overestimate the lift-to-drag ratio and have high values of $L/D > 4$ even for angles of attack exceeding $\alpha > 15°$. This is caused by their assumption that the kite flies at high angles of attack. We found that the angles of attack the kite is flying at are lower and do

10   usually not exceed $\alpha = 15°$. The two states of the depowered ($u_p < 0.5$) and the powered kite ($u_p = 1$) show different trends. We can see from Fig. 12 that the lift-to-drag ratio of the depowered kite depends mainly on the power setting u_p. Changes of angle of attack don't have a strong effect in this flight regime. For the powered kite where the power setting is kept constant at $u_p = 1$ the angle of attack is dominating the lift-to-drag ratio. The higher α is, the lower values we see for L/D.

The difference in lift-to-drag ratio of the kite for different power settings is large as can be seen in Fig. 14. The wing twist of

15   the kite as well as its anhedral angle is changed when the kite is depowered. Due to the complex and large-scale deformation

of the kite it seems justified to deal with the powered and depowered kite as two different wings rather than seeking to find one aerodynamic model with L/D only depending on the angle of attack. The idea of Fechner et al. (2015) and Ruppert (2012) to combine power setting and measured angle of attack in one variable is still used in Fig. 15.

4.4 Lift coefficient C_L

5   In Fig. 16 the lift coefficient is plotted against the measured apparent flow velocity for the kite in traction phase with the criteria that the value of the traction force is above $F_t = 3$ kN. Flight situations which do not meet this criteria mark transitions to/from the reel-in period or sharp turning maneuvers. Because of the constant force condition all points lie on a curve that fulfills
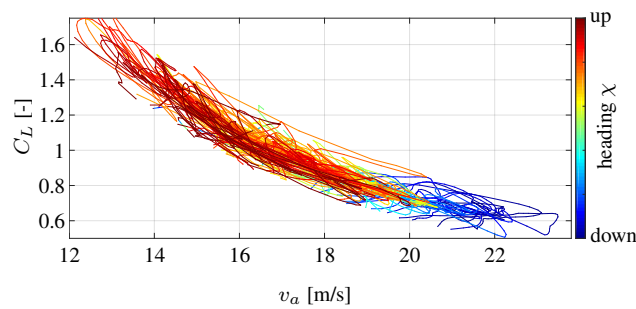
Figure 16. Dependency of the kite's equilibrium speed on the kite's heading χ. The kite is controlled to deliver a constant tether force of $F_t = 3.25$ kN.

$$C_L v_a^2 = \text{const.} \tag{12}$$

The constant force control strategy requires that the kite delivers a constant traction force of $F_{t,reel-out} = 3.25$ kN at the
10   ground station throughout the traction phase, regardless of atmospheric wind and flight situation such as elevation and heading. This goal is achieved by controlling the reel-out speed of the kite v_t. Whenever the traction force drops below $F_{t,reel-out}$, v_t is reduced, if it exceeds this value, v_t is increased. The interest of Fig. 16 is the fact that the kite chooses different flight conditions to produce the commanded force $F_{t,reel-out}$. When the kite is flying downward, it flies faster with a lower lift coefficient and angle of attack. When flying upward, the kite flies slower with a higher lift coefficient and higher angle of attack. This can
15   be explained by the effect of the kite's weight (see Fig. 8). When the constant force control strategy is applied, v_a exhibits an opposite trend compared to α and C_L. The opposite trend of angle of attack and apparent flow velocity v_a can also be observed in the plot of Fig. 10.

        During traction phase the kite flies with different angles of attack but the power setting is kept constant at $u_p = 1$. This way the change of C_L and L/D can be linked to the difference in α as the wing is not being actively deformed by changing u_p.
20   Figure 17 shows the lift coefficient with the angle of attack. The black points are the mean values for different headings χ. Thereby the ten black circles each represent the average of data points with a similar heading. The leftmost point is thus the average of all points where the kite's heading is most aligned with the gravity vector which are shown in dark blue in Fig. 17. Although the data is spread over a wide range, there are two clear trends visible:
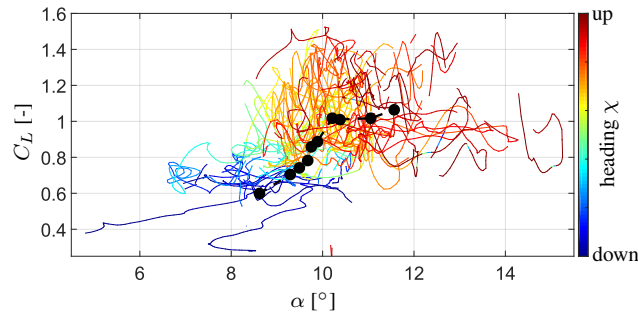
Figure 17. Lift coefficient C_L plotted over the angle of attack α. Black dots represent the mean values for different headings.

- – For higher angles of attack the lift coefficient is higher.

- – When flying upward the kite flies at a higher angle of attack and lift coefficient.

The first one is common behavior for a wing, the second one originates in the constant force control strategy and was already observed in (Oehler, 2017). The slope of the lift coefficient with increasing angle of attack is steep. In Fig. 17 the lift coefficient

5   increases from 0.7 at $\alpha = 9°$ to 1.0 at $\alpha = 12.5°$ which is close to the ideal case of a two-dimensional lifting surface. For wings with low aspect ratio such as a soft kite we generally expect a much smaller slope of the lift coefficient. Increased camber for higher angles of attack and flattening of the wing are two mechanisms that can contribute to this steep slope. The wing flattens for a higher C_L and therefore produces more lift. Since for the calculation of the lift coefficient we use a constant reference surface this would in return increase C_L.

10   During traction phase we do not change the power setting of the kite and can therefore not actively control α. The angle of attack it flies at is the result of the quasi-steady force equilibrium of the kite. The parameter with the biggest influence on the angle of attack is found to be the heading of the kite χ. When it is flying upward, drag and weight are almost aligned, for downward flight, they point in different directions. This causes the differences in apparent flow speed (see Fig. 16) and angle of attack (see Fig. 17).

15   **5   Conclusions**

The lift-to-drag ratio L/D of a soft kite can be determined during dynamic flight maneuvers with a flow direction sensor installed in the bridle lines. The power setting u_p and the angle of attack are found to have the most significant effect on the lift-to-drag ratio. The experimental data shows that L/D increases with the power setting u_p. The highest lift-to-drag ratio is reached for straight flight at a moderate lift coefficient C_L and angle of attack of $\alpha = 8°$. Steering maneuvers have a negative

20   effect on the lift-to-drag ratio.

In the observed flight the angle of attack varies only by around $8°$ during traction phase. Angle of attack and apparent flow velocity show opposite trends when the tether force is kept constant. Throughout the traction phase the kite shows a high lift

coefficient with high angles of attack while the kite's weight and heading have a considerable effect on these two variables. This effect is observed when the kite is flying upward: it flies at low speed and high angle of attack to compensate for gravity.

The power setting and angle of attack should be considered separately to accurately capture the aerodynamic behavior over the whole flight envelope. A change in power setting causes a complex deformation of the wing and thereby affects the

5 aerodynamic coefficients, while a change in angle of attack affects the aerodynamic coefficients by changing the flow field.

Establishing a dependency on both or dealing with the powered and depowered kite as two different wings seems necessary for a better aerodynamic model of a pumping cycle AWES.

The kite control unit has a considerable effect as it contributes about 40% of the kite mass and 10% of the drag. Having it suspended in the steering lines allows it to perform unpredictable movements especially during turns and when the tether force

10 is low during reel-in. This adds uncertainty to the calculated orientation of the kite. Moving the KCU into the bridle point and connecting it to both power and rear bridle lines could avoid this problem and results in an easier bridle model (Fig. 9).

Data availability. The dataset of this flight test is freely available for research purposes by contacting data@kitepower.nl.

Appendix A: Correction for flow velocity induced by the kite with lifting line theory
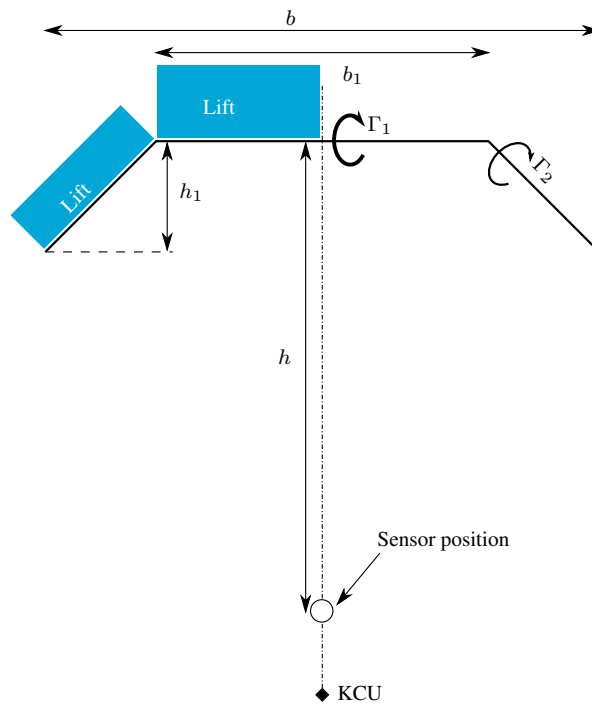
Figure A1. Simplified kite model with sensor position to apply lifting-line theory

In Fig. A1 the kite is flying out of the plane, the induced velocity v_{ind} in flight direction can be calculated using potential flow theory and the Biot-Savart-law.

$$v_{ind} = \frac{\Gamma}{4\pi r}\left(\cos\alpha_1 - \cos\alpha_2\right)$$

The induced velocity is the sum of induction by the circulation of the middle section Γ_1 and the tip section Γ_2. Γ_1 and Γ_2 can
5 be calculated with the values from Table A1.

$$v_{ind,sensor} = v_{ind,1} + v_{ind,2}$$

For symmetry reasons we calculate only one half and double the effect since both sides have the same effect on the induced velocity. For the velocity induced by the middle section we obtain

$$v_{ind,1} = 2\frac{\Gamma_1}{4\pi h}\cos\left[\arctan\left(\frac{2h}{b_1}\right)\right],$$

10 for the two tip sections we get

$$v_{ind,2} = \frac{2\sqrt{2}\Gamma_2}{4\pi\left(h + \frac{b_1}{2}\right)}\left\{\cos\left[\frac{3}{4}\pi - \arctan\left(\frac{2h}{b_1}\right)\right] - \cos\left[\frac{3}{4}\pi - \arctan\left(\frac{2(h-h_1)}{b}\right)\right]\right\}.$$

The freestream velocity v_∞ is the sum of measured apparent flow velocity v_a and v_{ind}. For the geometry of the used kite and sensor the induced velocity stays smaller than $v_{ind} < 0.2$ m/s. The induced angle of attack at the sensor's position α_i when considering the induced downwash of the kite's tip vortices stays below $\alpha_i < 0.6°$. Because of their small magnitude and to

Table A1. Model parameters of the V3 kite for lifting-line theory

b	b_1	h	h_1	$\frac{\Gamma_2}{\Gamma_1}$	L	$\overline{v_\infty}$
8 m	4 m	8.5 m	2 m	5/8	3250 N	18 m/s

15 simplify our calculations in this paper the measured apparent flow variables are considered always equal to the free stream velocity. For bigger kites that have an increased surface area and much higher pulling forces the induced velocity plays a bigger role and must be considered for a precise measurement.

Competing interests. Roland Schmehl is co-founder of and advisor for the start-up company Kitepower B.V. which commercially develops a 100 kW kite power system and which provided their test facilities and staff for performing the in situ measurements described in this article.
20 Both authors are financially supported by the EU H2020 project REACH, which also funds Kitepower B.V.

Acknowledgements. This project has received funding from the European Union's Horizon 2020 research and innovation programme under the Marie Skłodowska-Curie grant agreement No. 642682 for the ITN project AWESCO and the grant agreement No. 691173 for the "Fast Track to Innovation" project REACH. The authors appreciate the help from the team of Kitepower B.V.

References

Borobia, R., Sanchez-Arriaga, G., Serino, A., and Schmehl, R.: Flight Path Reconstruction and Flight Test of Four-line Power Kites, Journal of Guidance, Control, and Dynamics, accepted for publication, 2018.

Bosch, A., Schmehl, R., Tiso, P., and Rixen, D.: Nonlinear Aeroelasticity, Flight Dynamics and Control of a Flexible Membrane Traction

5   Kite, in: Airborne Wind Energy, edited by Ahrens, U., Diehl, M., and Schmehl, R., Green Energy and Technology, chap. 17, pp. 307–323, Springer, Berlin Heidelberg, https://doi.org/10.1007/978-3-642-39965-7_17, 2013.

Bosch, A., Schmehl, R., Tiso, P., and Rixen, D.: Dynamic nonlinear aeroelastic model of a kite for power generation, Journal of Guidance, Control and Dynamics, 37, 1426–1436, https://doi.org/10.2514/1.G000545, 2014.

Breukels, J.: An Engineering Methodology for Kite Design, Ph.D. thesis, Delft University of Technology, http://resolver.tudelft.nl/uuid:

10   cdece38a-1f13-47cc-b277-ed64fdda7cdf, 2011.

Bungart, M.: Fluid-Struktur Kopplung an einem RAM-Air-Kiteschirm, Master's thesis, University of Stuttgart, 2009.

Costa, D.: Experimental Investigation of Aerodynamic and Structural Properties of a Kite, Master's thesis, ETH Zurich, 2011.

Dadd, G. M., Hudson, D. A., and Shenoi, R. A.: Comparison of two kite force models with experiment, Journal of Aircraft, 47, 212–224, https://doi.org/10.2514/1.44738, 2010.

15   de Wachter, A.: Deformation and Aerodynamic Performance of a Ram-Air Wing, Master's thesis, Delft University of Technology, http://resolver.tudelft.nl/uuid:786e3395-4590-4755-829f-51283a8df3d2, 2008.

Diehl, M., Leuthold, R., and Schmehl, R., eds.: The International Airborne Wind Energy Conference 2017: Book of Abstracts, University of Freiburg | Delft University of Technology, Freiburg, Germany, https://doi.org/10.6094/UNIFR/12994, 2017.

Dunker, S.: Ram-Air Wing Design Considerations for Airborne Wind Energy, in: Airborne Wind Energy, edited by Ahrens, U., Diehl, M.,

20   and Schmehl, R., Green Energy and Technology, chap. 31, pp. 517–546, Springer, Berlin Heidelberg, https://doi.org/10.1007/978-3-642-39965-7_31, 2013.

European Commission: Resource Efficient Automatic Conversion of High-Altitude Wind (REACH), https://cordis.europa.eu/project/rcn/199241_en.html, accessed 1 June 2018, 2015.

Fechner, U. and Schmehl, R.: Flight path planning in a turbulent wind environment, in: Airborne Wind Energy, edited by Ahrens, U., Diehl,

25   M., and Schmehl, R., Green Energy and Technology, chap. 15, pp. 361–390, Springer Singapore, Springer Nature Singapore Pte Ltd., https://doi.org/10.1007/978-981-10-1947-0, 2018.

Fechner, U., van der Vlugt, R., Schreuder, E., and Schmehl, R.: Dynamic Model of a Pumping Kite Power System, Renewable Energy, https://doi.org/10.1016/j.renene.2015.04.028, 2015.

Hassig, H. J.: An approximate true damping solution of the flutter equation by determinant iteration, Journal of Aircraft, 8, 885–889,

30   https://doi.org/10.2514/3.44311, 1971.

Hobbs, S. E.: Kite performance measurements in natural wind, The Aeronautical Journal (1968), 94, 59–66, https://doi.org/10.1017/S0001924000022442, 1990.

Hummel, J.: Automatisierte Vermessung und Charakterisierung der dynamischen Eigenschaften seilgebundener, vollflexibler Tragflächen, Ph.D. thesis, Technical University Berlin, https://doi.org/10.14279/depositonce-5863, 2017.

35   Jann, T. and Greiner-Perth, C.: A New Type of Airflow Sensor for Gliding Parachutes, in: 24th Aerodynamic Decelerator Systems Conference (at AVIATION 2017), https://doi.org/10.2514/6.2017-3880, 2017.

Kite Power Systems: http://www.kps.energy/, accessed 25 May 2018.

Kitepower: http://www.kitepower.nl/, accessed 25 May 2018.

Kitepower: A 40 Square Meter Success, https://kitepower.nl/a-40-square-meter-success/, accessed 1 June, 2018.

Oehler, J.: Measuring apparent flow vector on a flexible wing kite, Master's thesis, University of Stutgart, https://doi.org/10.18419/opus-9890, 2017.

5   Oehler, J. and Schmehl, R.: Experimental Characterization of a Force-Controlled Flexible Wing Traction Kite, in: Book of Abstracts of the International Airborne Wind Energy Conference 2017, edited by Diehl, M., Leuthold, R., and Schmehl, R., pp. 122–123, University of Freiburg & Delft University of Technology, Freiburg, Germany, http://resolver.tudelft.nl/uuid:ec74a4f5-22ac-4d40-9b5d-8441b817019a, 2017.

Oehler, J., van Reijen, M., and Schmehl, R.: Experimental investigation of soft kite performance during turning maneuvers, Journal of
10   Physics: Conference Series, 1037, 052 004, http://stacks.iop.org/1742-6596/1037/i=5/a=052004, 2018.

Python, B.: Methodology Improvement for Performance Assessment of Pumping Kite Power Wing, Master's thesis, École Polytechnique Fédérale de Lausanne, http://resolver.tudelft.nl/uuid:462bba8d-e0ca-419d-a3b0-aaa93c284625, 2017.

Ruppert, M. B.: Development and Validation of a Real Time Pumping Kite Model, Master's thesis, Delft University of Technology, http://resolver.tudelft.nl/uuid:56f1aef6-f337-4224-a44e-8314e9efbe83, 2012.

15   Schmehl, R.: Experimental setup for automatic launching and landing of a 25m2 traction kite, https://www.youtube.com/watch?v=w4oWs_zNpr8, accessed on 1 May 2018, 2014.

Schmehl, R., Noom, M., and van der Vlugt, R.: Traction Power Generation with Tethered Wings, in: Airborne Wind Energy, edited by Ahrens, U., Diehl, M., and Schmehl, R., Green Energy and Technology, chap. 2, pp. 23–45, Springer, Berlin Heidelberg, https://doi.org/10.1007/978-3-642-39965-7_2, 2013.

20   Schmehl, R., van der Vlugt, R., Fechner, U., de Wachter, A., and Ockels, W.: Airborne Wind Energy System, Dutch Patent Application 2,009,528, 2014.

Skysails Power: http://www.skysails.info/power/, accessed 25 May 2018.

Stevenson, J.: Traction Kite Testing and Aerodynamics, Ph.D. thesis, University of Canterbury, http://hdl.handle.net/10092/7688, 2003.

Stevenson, J., Alexander, K., and Lynn, P.: Kite performance testing by flying in a circle, The Aeronautical Journal, 109, 269–276,
25   https://doi.org/10.1017/S0001924000000725, 2005.

Stevenson, J. C. and Alexander, K. V.: Circular flight kite tests: converting to standard results, The Aeronautical Journal, 110, 605–614, https://doi.org/10.1017/S0001924000001469, 2006.

van der Vlugt, R.: Aero- and Hydrodynamic Performance Analysis of a Speed Kiteboarder, Master's thesis, Delft University of Technology, http://resolver.tudelft.nl/uuid:9e0c7a62-149c-4fab-8d27-afe15c1a8795, 2009.

30   van der Vlugt, R., Peschel, J., and Schmehl, R.: Design and Experimental Characterization of a Pumping Kite Power System, in: Airborne Wind Energy, edited by Ahrens, U., Diehl, M., and Schmehl, R., Green Energy and Technology, chap. 23, pp. 403–425, Springer, Berlin Heidelberg, https://doi.org/10.1007/978-3-642-39965-7_23, 2013.

van der Vlugt, R., Bley, A., Schmehl, R., and Noom, M.: Quasi-Steady Model of a Pumping Kite Power System, Accepted for publication in Renewable Energy, 2018.

35   van Reijen, M.: The turning of kites, Master's thesis, Delft University of Technology, http://resolver.tudelft.nl/uuid:5836c754-68d3-477a-be32-8e1878f85eac, 2018.

Weston, D.: EnBW joins kite-wind project, Windpower Monthly, 21 June 2018, https://www.windpowermonthly.com/article/1485686/enbw-joins-kite-wind-project, accessed 22 June 2018, 2018.